Materials & Design 214 (2022) 110358

Contents lists available at ScienceDirect

Materials & Design

journal homepage: www.elsevier.com/locate/matdes

Additive manufacturing of short carbon fiber-reinforced polyamide composites by fused filament fabrication: Formulation, manufacturing and characterization

Yahya Abderrafai [a], Mohammad Hadi Mahdavi [a], Facundo Sosa-Rey [a], Chloé Hérard [a], Ivonne Otero Navas [a], Nicola Piccirelli [b], Martin Lévesque [a], Daniel Therriault [a,*]

[a] Department of Mechanical Engineering, Polytechnique Montreal, Montreal, QC H3T 1J4, Canada
[b] Safran Composites, Safran Group, 33 Avenue de la Gare, Itteville 91760, France

HIGHLIGHTS

- The authors report a study that combine microstructural characterization, mechanical characterization, and analytical homogenization on custom-formulated polyamide 12-based composites for Fused Filament Fabrication 3D printing.
- The customized homogenization model, which considers the distribution of carbon fibers aspect-ratio and orientation, helps explain the role of carbon fiber sizing on elastic properties.
- The authors report improvement of mechanical properties due to the addition of a heated environment apparatus, with up to two times for strength on the printing pattern orthogonal to the loading direction.
- Overall, modulus has seen an increase of 530% and strength an increase of 115%.

GRAPHICAL ABSTRACT

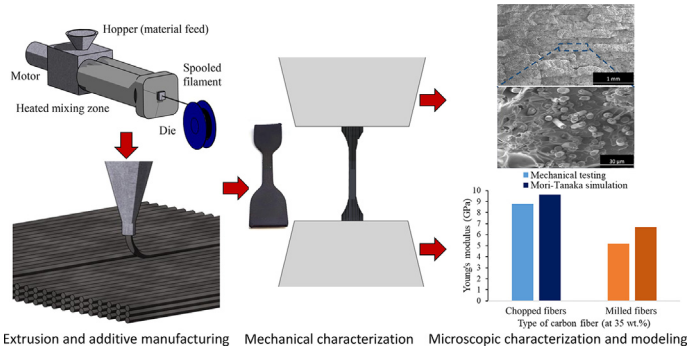

ARTICLE INFO

Article history:
Received 15 September 2021
Revised 21 December 2021
Accepted 23 December 2021
Available online 24 December 2021

Keywords:
FFF
Composites
Carbon fiber
Homogenization

ABSTRACT

Short carbon fiber-reinforced Polyamide 12 composite materials were prepared and used as filaments for additive manufacturing (AM) of structures using the Fused Filament Fabrication (FFF) method. The effect of carbon fibers concentration and type, infill pattern and environmental temperatures on mechanical properties of the printed test samples were investigated. The measured tensile modulus of the printed composite ranged from 1.4 to 8.8 GPa, an increase of up to 6.3 times the value of the neat printed polymer. The tensile strength ranged from 40 to 90 MPa, for an increase of up to 2.15 times. Optimization of the environmental temperature for improved coalescence of filaments led to a fair increase in values of the tensile modulus and strength, with an improvement up to 1.5 and 2 times, respectively, for the printed samples with pattern orthogonal to the loading directions. Microstructure characterizations were performed for mechanical results interpretations, with the help of a specialized homogenization model.

* Corresponding author.
E-mail address: Daniel.therriault@polymtl.ca (D. Therriault).

https://doi.org/10.1016/j.matdes.2021.110358

Micro-structural analysis
Mechanical characterization

The combination of FFF and carbon fiber-reinforced composite shows high promises for applications in the transportation industry.

1. Introduction

The additive manufacturing (AM) of reinforced polymer-based composites usually involves extrusion-based techniques such as Fused Filament Fabrication (FFF). The FFF process is carried out with an automated apparatus laying down molten thermoplastic filaments and relying on fusing them together to form a part. Since the melted polymer is deposited on top of an already solid polymer, poor fusing between filaments often occurs, leading ultimately to lower strength and lower elongation at break [1–3] than the same polymer produced by an injection process. However, the high shearing forces involved during the material extrusion induces preferential alignment in short fiber-reinforced composites, which typically results in higher mechanical properties along the printing direction [2,4,5]. While mechanical properties of FFF printed parts are weaker than those resulting from other manufacturing methods (e.g., injection molding, thermoforming), the process requires no capital investments to produce short series of geometrically complex parts, which makes it a preferable solution to other capital-intensive processes under these conditions. There is therefore a strong interest to investigate novel FFF feedstock materials and their manufacturing process parameters to deliver parts of superior mechanical properties.

The interface between filaments constitutes a source of weakness in 3D printed parts and the initiation site for delamination. Improvement of the filament interface adhesion could lead to an increase of the printed part overall strength. Yang et al. [6] demonstrated that this interface is highly influenced by the environmental temperature during printing.

Polyamides found many applications (e.g., gears, ball bearing) due to its toughness, its high ductility, its chemical resistance and relative low cost, when compared to other engineering polymers [7,8]. Polyamide 12 (PA12) in particular is also used by the transportation industry because of its lower moisture absorption, when compared to other polyamides [8]. PA12 is also the most widely used polymer for the Selective Laser Sintering method [4,9], but its utilisation in the FFF process is limited.

Carbon fibers (CF) are an important reinforcement for structural applications [10,11] because they exhibit very high specific mechanical properties (i.e., property over material density), and are widely available as continuous fibers, woven fabrics or short fibers [10,11]. When embedded into a polymer matrix, continuous fiber yields the highest specific stiffness in the direction along which they are aligned, when compared to fabrics or discontinuous fibers. However, continuous fiber composites are typically used in shell-like components with thin features [12]. Short carbon fibers are usually required in more geometrically complex structures, made by injection molding, compression molding or, more recently, by AM [4]. CF-reinforced thermoplastics for AM are mainly used for the tooling, functional prototyping and part replacement market [13]. Most CF-reinforced FFF feedstock exhibit tensile modulus below 7 GPa and a tensile strength below 60 MPa [14] with the maximal reported values of 13.8 GPa for tensile modulus in the case of reinforced ABS [5].

Few studies applied homogenization methods on these emerging composites materials. For example, Wang et al. [15] assessed the effect of porosity, Biswas et al. [16] predicted the orthotropic property of printed parts and finally Yao et al. [17] evaluated the effective properties of piezoelectric composites. So far, studies that predicted elastic properties based on the microstructure were only limited to injection molded composites. These studies focused on the microstructure characterization of composites where the orientation and length of carbon fiber are not homogeneously distributed in the matrix. Such methods were not yet applied to FFF-printed composites.

This work focuses on the evaluation of the mechanical performance of carbon fiber reinforced PA12 composites made by the FFF additive manufacturing process. The evaluation mainly consists of the effect of process parameters (i.e., environmental temperature) on mechanical properties, through tensile testing, SEM and CT-scan visualisation and a purpose-built homogenization model. The first section of the manuscript deals with the experiment and methods while the second sheds light on the results of mechanical and microscopic characterization of printed composites, informed by comparison with the modelling of the complex microstructure. We investigated the effect of the type and the concentration of carbon fibers, the effect of the environmental temperature on the composite's mechanical properties (i.e., tensile modulus and ultimate tensile strength (UTS)) and microstructure (i.e., fiber sizes and orientation, fiber sizing). The novelty of this paper lies in the combination all these elements into this in-depth analysis of a customized formulation, where the non-ideal distribution of fibers was integrated into a homogenization analysis to compare with experimental results.

2. Materials and methods

2.1. Homogenization model

Homogenization consists in predicting a composite's overall mechanical properties from the knowledge of the properties of its constituents. The implementation of the Mori-Tanaka homogenization model proposed by Benveniste et al. [18] performs an explicit orientation averaging on the contribution of each reinforcement, referred to in the sequel as inclusion, thus allowing the inclusions to have arbitrary orientation [18]. It has been shown that for this type of solid, the Mori-Tanaka model predicts effective properties that match the lower Hashin-Shtrikman bound for aligned continuous inclusion, and are even lower for any other orientation and aspect ratio distribution [19]. Furthermore, the Mori-Tanaka model assumes perfect interfaces between phases. For a distribution of cylindrical fibers, each having an orientation given by Euler angles ϕ and θ as shown in Fig. 1.c, and having aspect ratio R, the homogenized stiffness tensor C predicted by this model takes the form:

$$\mathsf{C} = \mathsf{C}_0 + \sum_{r=1}^{N} c_r P(\phi_r, \theta_r)(\mathsf{C}_r - \mathsf{C}_0) : \mathsf{A}_r(R_r), \tag{1}$$

where r denotes a particular phase ($r = 0$ for matrix, $r > 0$ for fibers), c_r is the volume fraction of phase r, $\mathbf{C}_r$ and $\mathbf{A}_r$ are the stiffness and localization tensors, respectively (bold Latin letters represent 4-th order tensors). $P(\phi, \theta)$ is defined as the projection operation for a 4-th order tensor, given by:

$$T'_{mnop} = P(\phi, \theta) T_{ijkl} = P_{im} P_{jn} P_{ko} P_{lp} T_{ijkl} \tag{2}$$

where Einstein summation has been used. P_{ij} is the rotated frame of reference tensor, computed in the ZYZ intrinsic Euler convention

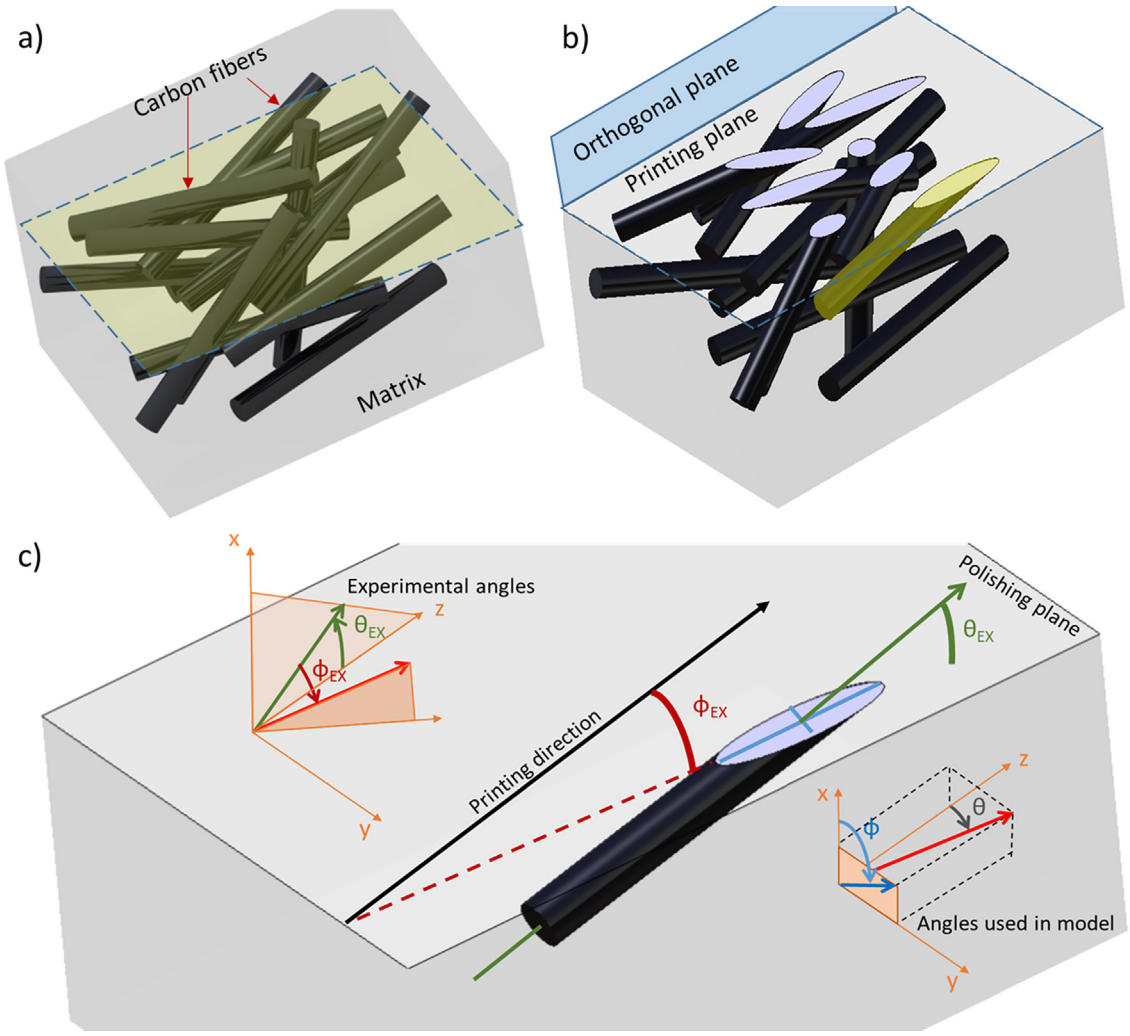

Fig. 1. Schematic explaining the different parameters for the calculation of the angular difference between carbon fibers and the printing direction. a) Schematic of polyamide matrix-embedded fibers before polishing. The polishing plane, in transparent yellow, is parallel to the printing plane. b) Schematic of a polished printed composite. The intersection of the polishing plane and a cylindrical fiber is an ellipse c) View of a single embedded fiber, and how the angles are measured on SEM images. The out-of-plane angle ϕ_{EX} is the angle between the fiber and the polishing plane. L is the semi-major axis of apparent ellipse, D is the semi-minor axis of apparent ellipse and diameter of the fiber and θ_{EX} is the In -plane angular variation between the fiber and the printing direction. (Extrinsic Euler angle convention).

$R_z(\phi)R_{y'}(\theta)R_{z''}(\rho)$, where $R_z(\phi)$ denotes a rotation of angle ϕ around axis *Z*. The next rotation is done with respect to the y axis of the rotated referential (denoted by y') and the final rotation $R_{z''}(\rho)$ is neglected as it rotates the fiber along its major axis. In each phase *r*, A_r becomes:

$$A_r = T_r : \left(\sum_{r=0}^{N} c_r T_r\right)^{-1}, \tag{3}$$

where $\mathbf{T}_r = \left[I + S_r^{\boldsymbol{E}}(R) : C_0^{-1} : (C_{\boldsymbol{r}} - C_0)\right]^{-1}$. Here, $S_r^{\boldsymbol{E}}$ is Eshelby's tensor for the phase

$r \neq 0$, which depends on C_0 and the aspect ratio *R* of the inclusions only. For an isotropic matrix and an ellipsoidal inclusion, $S_r^{\boldsymbol{E}}$ can be calculated with the help of the Green function as described by Michel et al. [20].

2.2. Materials and composites preparation

PA12 Grilamid® L20 Nat in pellet form was purchased from EMS-Grivory (Germany). According to the manufacturer, the polymer had an elastic modulus of 1400 MPa under dry conditions while its tensile strength was of 50 MPa when submitted to 1 mm/min tensile tests [21]. Milled (MCF) and chopped (CCF) carbon fibers (Panex35 with 95% carbon content) were purchased from Zoltek (USA). According to the manufacturer, the CCFs had an initial length of 6 mm and were coated with a sizing agent adapted for polyamides at a weight ratio of 2.75%, while the MCFs had an initial length of 150 μm and were not sized. CCFs and MCFs have the same intensive properties. The carbon fibers and PA12 pellets were compounded in a plastic extruder model LSM 30.34 from Leistritz© (Nuremberg, Germany). The extrusion process consisted of two extrusion steps performed under the same mixing conditions. The hopper zone (inlet) temperature was set to 185 °C and gradually increased to 240 °C in the mid-zone, and then decreased to 225 °C in the die (exit) zone. The screw speed was set at 36 rpm and the die diameter was 2.85 mm. The CFs and the PA12 pellets were fed to the extruder using separate feeders. The produced filament was cooled inside a water bath at room temperature and then cut in pellets with a pelletizer. The obtained composite pellets were extruded for a second time after drying overnight, and the obtained filament (1.75 ± 0.15 mm diameter) was passed through the water bath while two soft rollers of a calender machine pulled it. The filament diameter control was

achieved by regulating the calender machine's pulling speed. The filament was manually winded onto a spool. Six different composites were produced: neat PA12 and reinforced PA12 at 20, 35 and 40 wt% with MCFs (12.2, 23.1 and 27.1 vol%), and at 20 and 35 wt% with CCFs (12.2 and 23.1 vol%). These concentrations were chosen to provide a wide range of concentrations within the possible mixing range (limited to 40 wt%), while limiting the number of specimens produced. It was not possible to achieve a printable filament of CCF at 40 wt% as the required torque to process it was beyond our setup capabilities.

2.3. Additive manufacturing

The printing was performed using a Leapfrog Creatr Dual (Leapfrog™, Netherlands) 3D printer. The printer was equipped with a heated bed that moved in the *z* direction while the printer nozzle moved in $\times$ and *y* directions. Simplify 3D software (Simplify3D, USA) was used to slice the 3D models and to provide instructions for printing. Every specimen was printed with layers having a height of 0.2 mm, a 100% infill and no shell (top, bottom or lateral) as well as at a speed 50 mm/s with a 0.6 mm lubricated hardened-steel plated wear resistant nozzle Ubis-style (MicroSwiss, USA). The first layer was printed with a 50% decreased speed on a glue layer to promote adhesion to the glass bed and was added as a sacrificial layer in the part design. The glass bed and nozzle temperature were of 65 °C and 255 °C, respectively. The printing was carried out under different environmental temperatures. A chamber was designed to contain the 3D printer and control the temperature inside to up to a maximum of 65 °C. The heat was produced using heating elements with blowing air and controlled through a custom Arduino-based PID system. IR lamps were used as a supplementary heating source in order to heats up the chamber and turned off during printing.

ASTM D638 Type IV dogbone specimens were printed for mechanical testing. The specimens were identified with a unique letter referring to the printing direction with respect to the specimen's longitudinal axis. (L for length, W for Width). Dogbone specimen were printed with PA12/MCF and PA12/CCF according to L and W printing direction. In addition, another batch of specimen was printed with 35 wt% MCF according to the L and W printing direction for different environmental printing temperatures (22, 35, 50, 65 °C). The specimens were made of 16 printed layers, with an additional two sacrificial layers to be sanded at the top and bottom surfaces, which led to 3.6 mm thick specimens. Polishing was necessary for the DIC method which requires a very flat and smooth surface for painting the speckle pattern. Creating sacrificial layers, that were printed in a different direction than the tested one, allowed us to create that flat surface without damaging the studied orientation. In addition, the sanding step should not significantly affect the mechanical properties as it was performed using fine grit (i.e., grit 800). The specimens were then dried under vacuum conditions for $\sim$ 12 h at room temperature prior to mechanical testing.

2.4. Mechanical characterization

Tensile tests were performed in accordance with the ASTM D638 standard with an MTS Insight electromechanical testing machine (MTS, USA) using a 1 kN and a 50 kN load cell, testing at least 5 specimens for each measure. The stereoscopic Digital Image Correlation (DIC) technique was used for strain measurements using the Vic3D system and software (Correlated Solutions, USA). Specimens were covered by a white acrylic spray paint before adding the black speckle pattern with a stamp roller. The subset size ranged between 27 and 50 pixels to allow a delta uncertainty below 0.03 pixels. Sub-pixel interpolation was made using an optimized 8-tap with a zero-normalized squared differences criterion, while lagrangian strains were computed with a filter size of 15 pixels.

2.5. Microscopic characterization

Different sections of the tested specimens (i.e., fracture faces, grip section) were cut using an Isomet low speed cutter (Buehler, USA) at planes of interest before coating with a low temperature UV curable resin for handling. Grinding and polishing for SEM observations was performed using a Metaserv 2000 variable speed polisher (Buehler, USA), going successively through 320, 600 and 1000 Grit Silicon Carbide grinding papers before using polishing cloth and polycrystalline diamond suspension of 9, 3 then 1 μm, respectively. A final polishing cycle was carried out with 0.06 μm colloidal silica suspension. The specimens where thoroughly washed between each cycle and finally cleaned with an ultrasonic cleaner before being dried at room temperature in a vacuum enclosure before Scanning Electron Microscope (SEM) observation or Computed Tomography scans (CT-Scan). Dry fiber samples were also observed under the SEM to analyse the sizing composition.

The polished sections and the isolated fibers were imaged under a JEOL JSM7600F (Peabody, USA) SEM operated at an acceleration voltage of 5 kV. Energy dispersive X-Ray elemental analysis was performed to the CCF surface to characterize the sizing agent's chemical structure. SEM and light optical microscopy (LOM) studied the CCF and MCF aspect ratio distribution. LOM was carried out using an Olympus BX-61 (Olympus Inc, USA) microscope under different magnifications.

Printed fibers and structures were scanned, at high (0.7 μm) and medium (5 μm) resolution respectively, using a Zeiss Xradia 520 Versa CT-scan (Carl Zeiss, Germany). Scans of the structures printed at room temperature and 65 °C were studied to analyze the inter-filament bonding, while porosity was characterized for MCF and CCF-reinforced composite filaments. The thresholding method was used to visually identify the grayscale pixels belonging to the porosity. The number of pixels belonging to the porosities is compared to the total number of pixels to determine the porosities fraction in the printed composite material.

2.6. Fibers aspect ratio and orientation characterization and micromechanics predictions

Some of the composites prepared with MCF and CCF after FFF printing (three of each) were dissolved in sulfuric acid (H_2SO_4) for two days prior to any testing. Dissolution droplets were then placed on a glass slide covered with a copper conductive tape. The slides were placed under a fume hood for one week to evaporate the acid, followed by heating on a plate at 90 °C until complete acid evaporation was achieved. The samples were coated with gold to avoid electrostatic charge accumulation prior to SEM observation. Image analysis was performed using the software ImageJ (NIH, USA). The MCF and CCF lengths and diameters were each measured for $\sim$ 3000 fibers, using the Measure function included in the ImageJ software, before computing the aspect ratios by dividing the lengths by their respective diameters ($\sim$7.2 μm).

Fiber angles were measured with respect to the printing direction along two planes in the tensile specimens: the printing plane and its orthogonal plane containing the printing direction. The polishing plane is aligned with the printing plane. Fig. 1.a and b are schematics of a printed composite a) before and b) after a planar polishing. The intersection of a plane and a cylindrical fiber is an ellipse with parameters that are dependent on the orientation of the fiber. The Euler angles of fibers with respect to the coordinate system of the tensile specimen inside the matrix was determined by measuring the semi-axis of these ellipses. (The intrinsic *XYZ*

convention is used here, Z being the printing direction). Here we specify the subscript EX for experimental, to differentiate the ϕ and θ angles used in the Mori-Tanaka model, which use a rotation convention more commonly encountered in integration over spherical coordinates. The MCF and CCF angle distributions were each studied for 300 fibers, using the Measure function included in the software.

Fig. 1.c shows the in-plane angle θ_{EX} as the angle between the printing direction and the direction of the major semi-axis of the ellipse. The figure also shows the out-of-plane angle ϕ_{EX} as the angle between the fiber axis and the polishing plane. ϕ_{EX} was determined using the minor semi-axis measurement. Since the minor semi-axis of the ellipse is equal to the fiber diameter, the angle ϕ_{EX} formed by the fiber and the printing plane is equal to:

$$\phi_{EX} = cos^{-1}\left(\frac{D}{L}\right) - \frac{\pi}{2}, \tag{4}$$

with D and L being the minor and major semi-axes, respectively. Once the angles θ_{EX} , ϕ_{EX} and the aspect ratio R were obtained, the angles were converted into the intrinsic ZYZ convention, as detailed in supplementary Figure S1. Then, the distributions for the three variables where fitted with all the continuous probability distribution functions (PDFs) available in the Scipy Statistics library [22] and the best fit, in the sense of least squared error, was selected to represent each variable. With these PDFs, it becomes possible to transform equation (1) where $N-1$ discrete inclusions are summed, into:

$$\mathrm{C} = \mathrm{C}_0 + \frac{c_1}{4\pi}\int_0^{2\pi}\int_0^{\pi}\int_{R_{min}}^{R_{max}} \psi_R\psi_\phi\psi_\theta P(\phi,\theta)(\mathrm{C}_1 - \mathrm{C}_0) : \mathrm{A}(R)\sin\theta dR d\theta d\phi, \tag{5}$$

where ψ_ϕ, ψ_θ and ψ_R are the PDFs for ϕ, θ and R, respectively. Equation (5) considers the contribution of a single inclusion material (r = 1). This integration is performed by gaussian quadrature, as:

$$\mathrm{C} = \mathrm{C}_0 + \frac{c_1}{4\pi}\sum_{i_\phi=0}^{N_\phi}\sum_{i_\theta=0}^{N_\theta} w_\phi w_\theta \psi_\phi\psi_\theta \times \sin(\theta)P(\phi,\theta)\left(\sum_{i_R} w_R\psi_R(\mathrm{C}_1 - \mathrm{C}_0) : \mathrm{A}(R)\right), \tag{6}$$

where i_ϕ, i_θ and i_R are the values at which the quadrature is evaluated, and w_ϕ, w_θ and w_R are the weights of said quadrature. Note that w_θ refers to the value for w evaluated at $\theta = i_\theta\pi/N_\theta$, for $i_\theta = 0,\cdots,N_\theta$ and so on for all other terms that depend on θ,ϕ and R, i.e. w,ψ and **A**. The number of gauss quadrature points required to converge within 0.5% of the final values in C were: $N_\phi = 8$, $N_\theta = 256$ and $N_R = 64$. The exact parameters for each distribution are given in Appendix A.

3. Results and discussion

3.1. Effect of short fiber reinforcement on tensile modulus and strength

3.1.1. Microstructural observations: Sizing, fiber orientation and aspect ratio

Fig. 2.a shows a SEM micrograph of a pristine CCF that went through Energy-Dispersive X-ray spectroscopy (EDX), focused in the highlighted region. Fig. 2.b shows the EDX spectrum extracted from the sizing agent observed on the carbon fiber. The spectrum reveals the presence of silicon and sodium, suggesting the use of a silane coupling agent, a type of sizing that has been reported as efficient on polyamide matrices [23,24].

Fig. 3.a and 3.b show SEM micrographs of a CCF-reinforced printed specimen taken along and perpendicular to the printing direction, respectively. They both show the presence of white spots whose chemical composition corresponds to that of the assumed sizing agent, determined with the EDX. These spots are not visible in Fig. 3.c and 3.d that show the micrograph of MCF reinforced specimen. These observations suggest that due to the heat generated during the mixing process, the sizing surrounded the CCFs and blended into the matrix. The figure also shows that the sizing agent is seemingly responsible for ensuring a proper adhesion between the matrix and CCF, whereas some empty space exists at the interface between the matrix and the MCF when no sizing agent is present, as observed in Fig. 3.c and 3.d.

Fig. 4.a, b and c show the distribution of the aspect ratio and the orientation of the fibers for the composites made of MCF and CCF in histogram form. Fig. 4.a shows that there is no preferential alignment in the plane normal to the printing direction (azimuthal angle ϕ has a uniform distribution) and Fig. 4.b suggests that there is a slight difference between the fiber angles distributions for the composites made of MCF and CCF for the elevation angle θ, with means of 15.0° and 16.8° and 75% of the distribution below 19.5° and 21.3° for CCF and MCF-made composites, respectively**.** The CCF appears to be more present at low angles ranges since 40 % of the CCF are oriented with an angle below 11.0°, when compared to 33% of the MCF that are oriented at an angle lower than 11°.

Fig. 4.c shows that the MCF exhibits smaller aspect ratios, with 76% of the MCF population below a ratio of 5, while this ratio is close to 33% in the CCF case. 9% and 34% of the MCF and CCF, respectively, have aspect ratios ranging from 5 and 10. These observations suggest that CCF have, on average, higher aspect ratios than the MCF. By considering that the composites made of CCF have their fibers more closely oriented to the printing directions than the composites made of MCF, it is expected that the resulting axial stiffness of the composites made of CCF will be greater than that of the composites made of MCF. Moreover, since CCF have higher aspect ratios, these fibers are more prone to shear-induced alignment in the molten state of the matrix [25], which could explain the measured orientation distributions of CCF and MCF.

When undergoing mixing with a polymer, the chopped carbon fibers length is significantly reduced from 6 mm (aspect ratio of $\sim$ 833) to lengths corresponding to aspect ratios ranging from 1 to 20. The reason for that stems from the high shear stresses occurring inside the twin screw extruder necessary for the mixing. These observations make the control of the size of fibers inside the matrix a critical condition to master manufacturing of high performance printed thermoplastic composites. Future blends should focus on achieving longer lengths to allow higher moduli and UTS.

Additional observation on the matrix shows that the material porosity, excluding the 3D printing-related porosity, was measured to be 0.6% for the CCF-reinforced specimens while being around 0.1% in the case of MCF specimens, suggesting a negligible impact of the porosity on the mechanical properties, which has been omitted in the homogenization model.

3.1.2. Fiber weight percent

Fig. 5 shows the average strain-stress responses for L oriented MCF and CCF reinforced specimens, as well as the neat resin-normalized tensile modulus and ultimate tensile strength (UTS), with respect to the mass fraction of carbon fiber and its type. The maximal elongation at break of neat resin specimens is much higher than for all the composites (25% for neat resin, when compared to 3 to 8% and 3 to 4% for MCF and CCF-reinforced specimens, respectively). However, the composite specimens exhibit significantly higher tensile modulus and strength, with increases of up to 5.5 times the original value, from 1.6 GPa (standard deviation

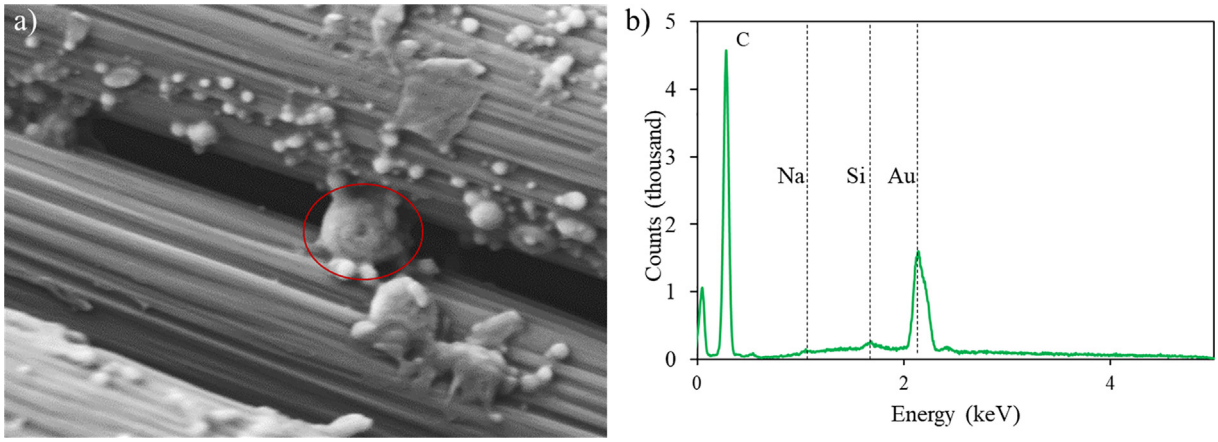

Fig. 2. Characterization of the sizing a) SEM micrograph of pristine CCFs with its sizing identified by a red circle b) EDX spectrum of the highlighted region of subfigure a). The identified sizing agent found on the fiber's surface contains silicon and sodium, suggesting the presence of silane coupling agent.

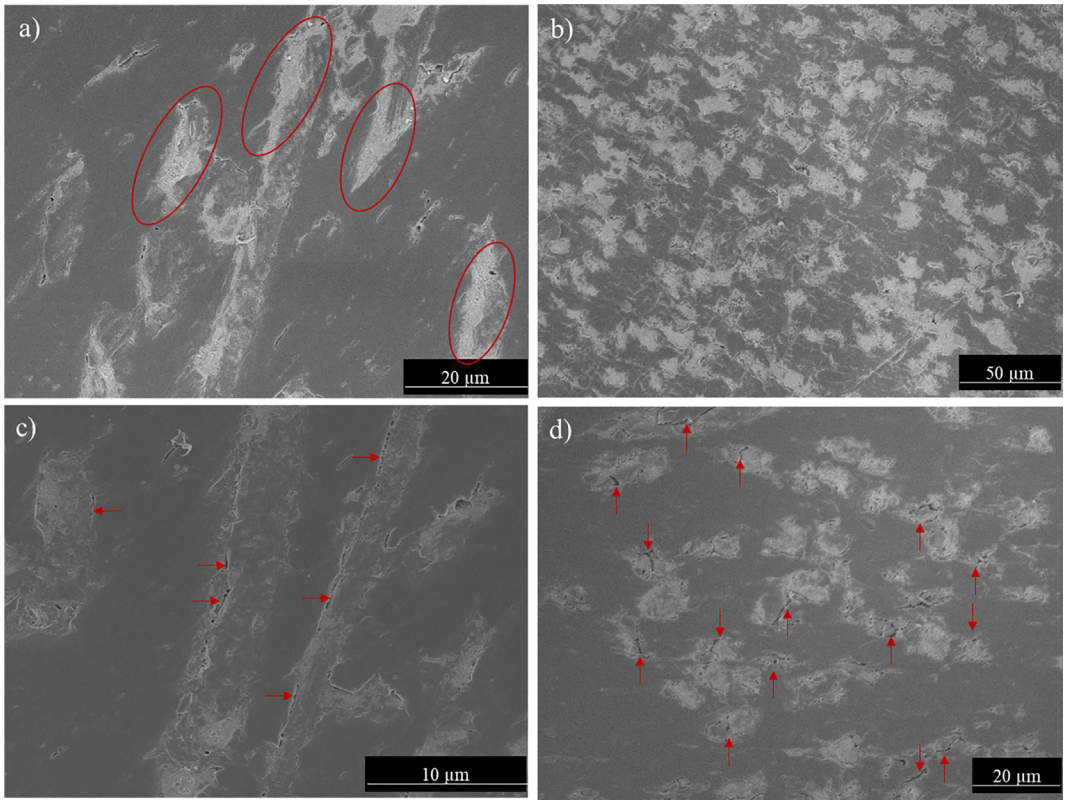

Fig. 3. SEM micrographs of polished printed reinforced PA samples: a) CCF-reinforced specimen along the printing direction (high magnification) b) CCF-reinforced specimen orthogonal to the printing direction c) MCF-reinforced specimen along the printing direction d). MCF-reinforced specimen orthogonal to the printing direction. These micrographs show the alignment of carbon fibers in the printing direction (a and c) and the spread of sizing along the fiber/matrix interface for the CCF (circled in a) and the cracks at the fiber/matrix interface (marked with red arrows in c and d).

of 0.03 GPa) to 8.8 GPa (standard deviation of 0.22 GPa), for tensile modulus and up to 2 times the original value, from 44 MPa (standard deviation of 0.5 MPa) to 89 MPa (standard deviation of 4.2 MPa), for the UTS of 35 wt% CCF-reinforced specimens. There is a clear correlation between the increase in carbon fiber loading and the increase in tensile modulus and UTS. This reinforcement phenomenon is a typical effect of carbon fiber addition, as supported by micromechanics theories [11]. Also, there is a tensile modulus increase to 4.3 times and UTS increase to 1.8 times the original values for 20 wt% CCF-reinforced composites, when compared to 3.5 times and 1.38 times for tensile modulus and UTS, respectively, for 40 wt% MCF-reinforced. These observations suggest that a 20 wt% CCF-reinforced sample shows a higher increase of properties as that observed for the 40 wt% MCF-reinforced composites. Overall, CCF-reinforced printed composites performed better than their milled counterparts, even though both carbon fibers types were provided by the same manufacturer and were made from the same carbon material with the same mechanical properties. The discrepancies in properties between MCF and CCF-reinforced printed composites could be due to different factors,

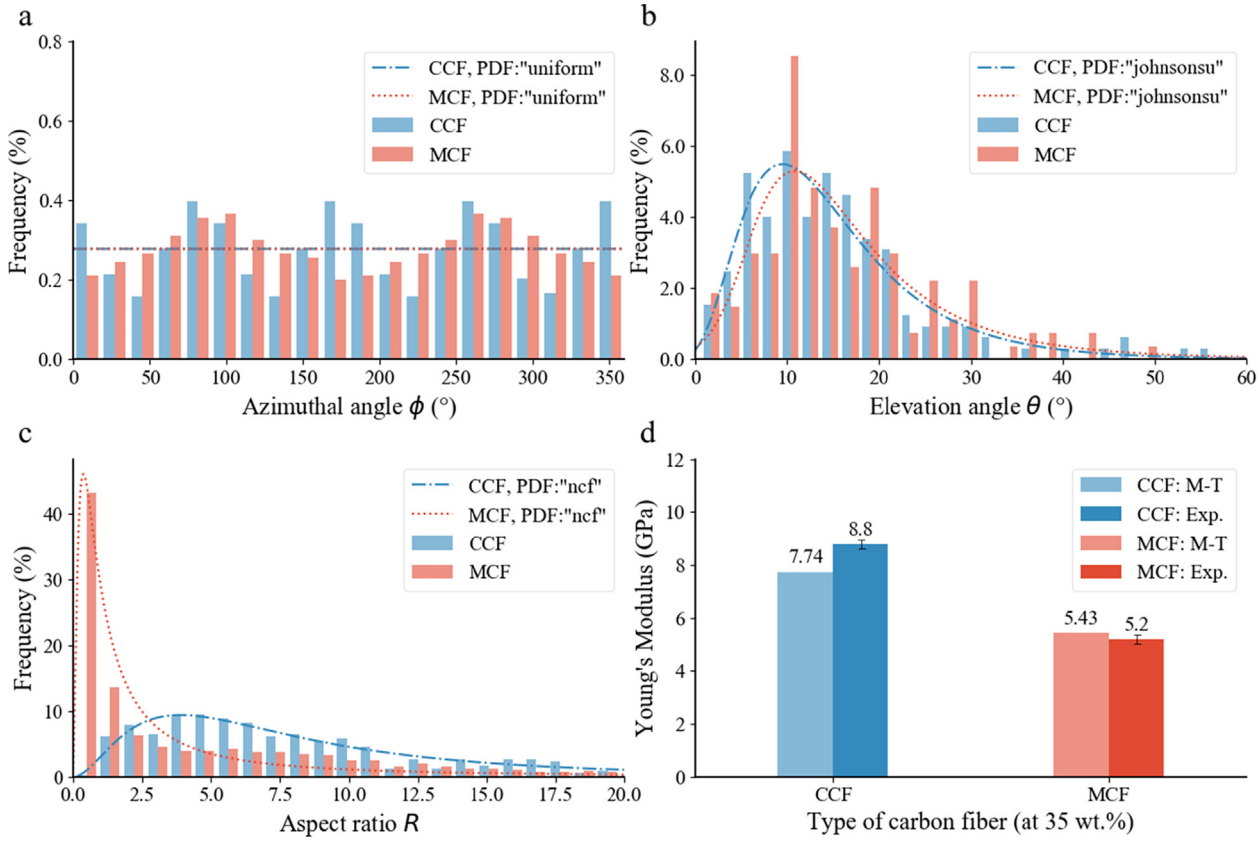

Fig. 4. Histogram and probability density functions (PDFs) of: a) azimuthal angle ϕ and fitted uniform distribution, (b) elevation angle θ and fitted Johnson's SU distribution and (c) aspect ratio R for CCF and MCF in the printed composites and fitted non-central F distribution. d) Comparison of tested tensile modulus with the Mori-Tanaka-predicted tensile modulus for CCF and MCF printed composites at 35 wt% concentration. The difference between the experimental and predicted longitudinal tensile modulus is larger for CCF (14%) than for MCF (5%).

but the importance of the effect of the sizing on the mechanical properties cannot be confirmed without an analysis accounting the composite microstructure. But since orientation and lengths distribution are both different for CCF and MCF, ascertaining the effect of sizing alone would require another round of testing.

It should be noted that such level of increase in modulus and UTS in FFF printed composites is consistent with data available in the literature, such as in the case of ABS with carbon fiber reinforcement [5]: the tensile modulus and strength of an ABS composite has seen a six-fold and two-fold increase, respectively, at a 30 wt% loading of carbon fiber.

3.1.3. Mori-Tanaka prediction and sizing effect on mechanical properties

Fig. 4.d shows Mori-Tanaka (MT) Young's modulus prediction for CCF and MCF-reinforced composites for weight fraction of 35 % (equal to a volume fraction of 23.1% for 1.81 density) using the measured data on fiber aspect ratio R and orientation ϕ and θ, assuming an ideal interface between matrix-fiber. The MT model also relies on the manufacturer-provided carbon fiber modulus of 242 GPa. In addition, the transverse modulus as well as the two Poisson's ratios and the shear modulus required to construct the transversely isotropic C_1 tensor of the carbon fiber are 24.8 GPa, 0.256, 0.3 and 27.3 GPa respectively, as reported by Miyagawa et al, [26]. The average measured tensile modulus for CCF-reinforced specimen in the L configuration is 8.8 GPa (standard deviation of 0.22 GPa) and the MT simulation predicts a module of 7.74 GPa. This represent a difference of 14%, while in the case of the MCF, the measured tensile modulus is 5.2 GPa (standard deviation of 0.089 GPa) and the simulated is 5.45 GPa, representing a smaller difference of 5%. In the ideal case of continuous (infinite) and perfectly aligned reinforcements, the Mori-Tanaka method is expected to converge on the lower Hashin-Shtrikman bound of the actual value. Since inclusions here are not continuous nor aligned, it is expected that the result of the Mori-Tanaka method will be even lower for this case. Since both aspect ratio and orientation distributions are accounted for in the same manner for CCF and MCF composites, we assume that the fact that the predicted tensile modulus is higher rather than lower than the measured value for MCF-reinforced specimens can be attributed to the absence of sizing for this type of composite. If the lack of sizing reduces the composite the experimentally measured stiffness with respect to that predicted by the homogenization model, the measured value for the tensile modulus could be lower than the Mori-Tanaka estimate. In the presented case, it shows that this silicon and sodium-based sizing is beneficial to the mechanical properties when used in a polyamide matrix, compared with using no sizing. Mori-Tanaka homogenization provides lower bounds for mechanical effective properties. As such, having elastic properties below that lower bound could be an indicator of an imperfect adhesion, granted that all possible factors are accounted for (i.e., angular and aspect ratio distributions). Experimentally measuring elastic properties slightly higher than those predicted by the Mori-Tanaka model does not imply a better adhesion since the Mori-Tanaka provides a lower bound estimate. According to our knowledge, our analysis is the first study considering the real distribution of fiber orientation and aspect ratio of short-fiber composites printed by FFF.

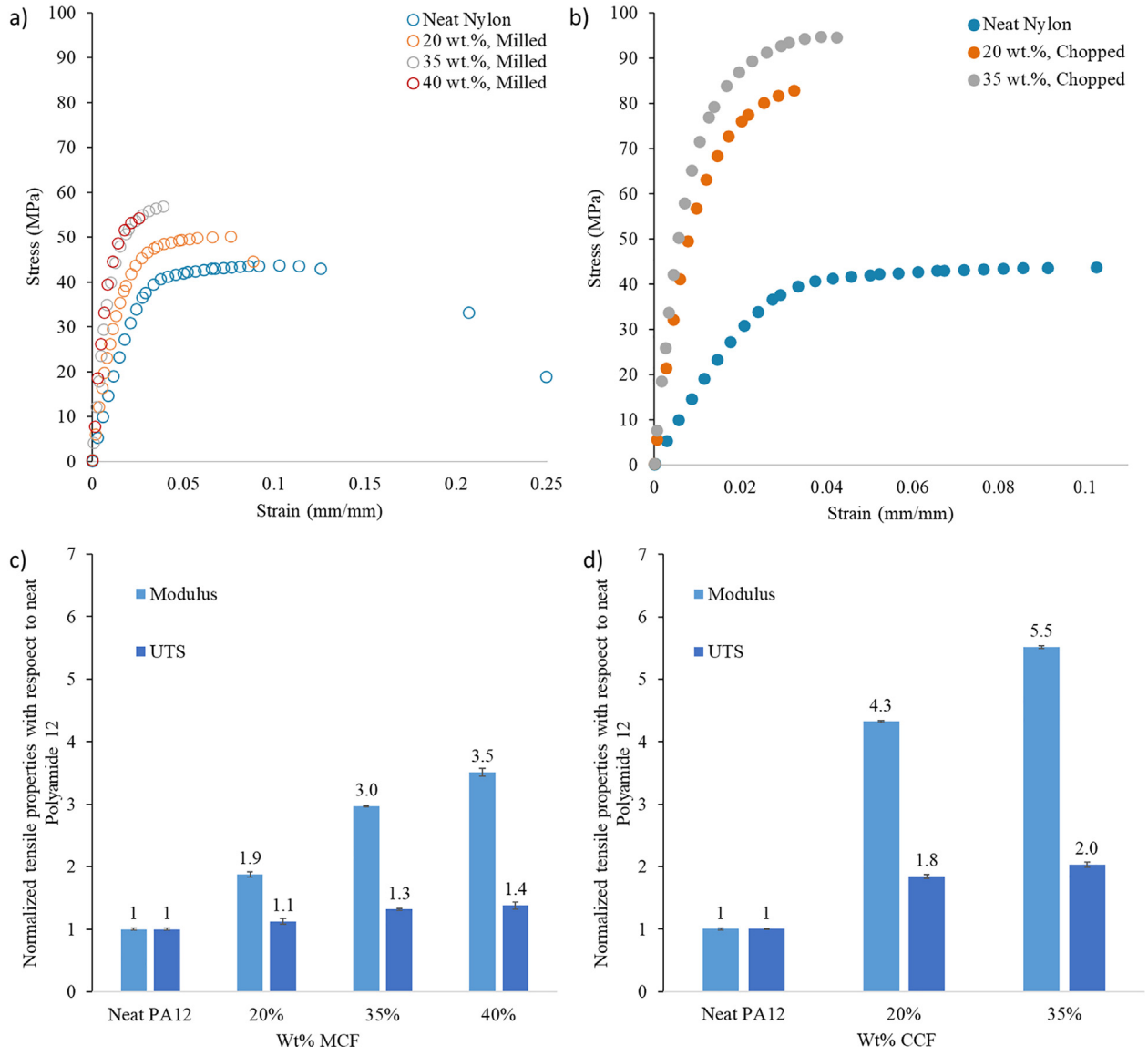

Fig. 5. Mechanical properties of reinforced PA with respect of type and weight concentration of carbon fiber a–b) Average stress-strain curve responses for L specimens with respect to type and weight percentage of carbon fiber: a) MCF and b) CCF. c–d) Normalized mechanical properties in L specimen with respect to type and weight percentage of reinforcement: c) MCF and d) CCF. The addition of carbon fibers improves the strength and the tensile modulus at the expense of elongation at failure, with the CCF being more efficient than the MCF: at 35 wt%, CCF specimens have a modulus and UTS 5.5 times and 2 times that of the neat PA12, respectively, while MCF have 3 times and 1.3 times the values of the neat polymer.

3.2. Effect of environmental printing temperature

Fig. 6 shows the evolution of the a) Tensile modulus and b) UTS in specimens printed along the L and W directions as a function of the environmental temperature, for a 35 wt% MCF-reinforced PA12. For specimens printed along the L and W directions, a noticeable increase in properties is seen between 22 °C (room temperature) and 35 °C, with increases to 1.36 times and 1.68 times for tensile modulus and UTS, respectively, when compared to the values measured on specimen printed in an environment at 22 °C, for the W specimen. The properties improved further as the temperature was increased, but somewhat more slowly: at 65 °C for the specimens printed in the W direction, tensile modulus increased to 1.41 times the original tensile modulus value (i.e., from 2.2 GPa (standard deviation of 0.03 GPa) to 3.1 GPa (standard deviation of 0.25 GPa)) and UTS 1.83 times the original UTS value (i.e., 24 MPa (standard deviation of 0.6 MPa) to 44 MPa (standard deviation of 4 MPa)). This is the most significant improvement observed. Specimens printed in the L direction exhibited lower benefits when using a heated environment at 65 °C compared to room temperature, with increases to 1.1 times and 1.3 times for tensile modulus (from 5.1 ± 0.31 to 5.6 ± 0.2 GPa) and UTS (from 45.9 ± 4 to 59.7 ± 0.6 MPa), respectively. While it can be observed that the higher the environmental temperature the higher the tensile modulus and strength, most of the increase in properties is reached for a printing environment of 35 °C. While the setup did not allow to go at higher environmental temperature, the increase in properties should be less noticeable until reaching the vitreous transition temperature, around 80 °C. Such results are corroborated by findings in the literature [27], where higher ultimate tensile strength is correlated to higher printing environmental temperature. It should be noted, however, that the literature is scarce regarding the bonding mechanisms involved in FFF.

Fig. 6.c is a SEM image of a typical break surface of 3D printed specimen, with the cross-section perpendicular to the filament orientation. The figure shows that there is significant delamination

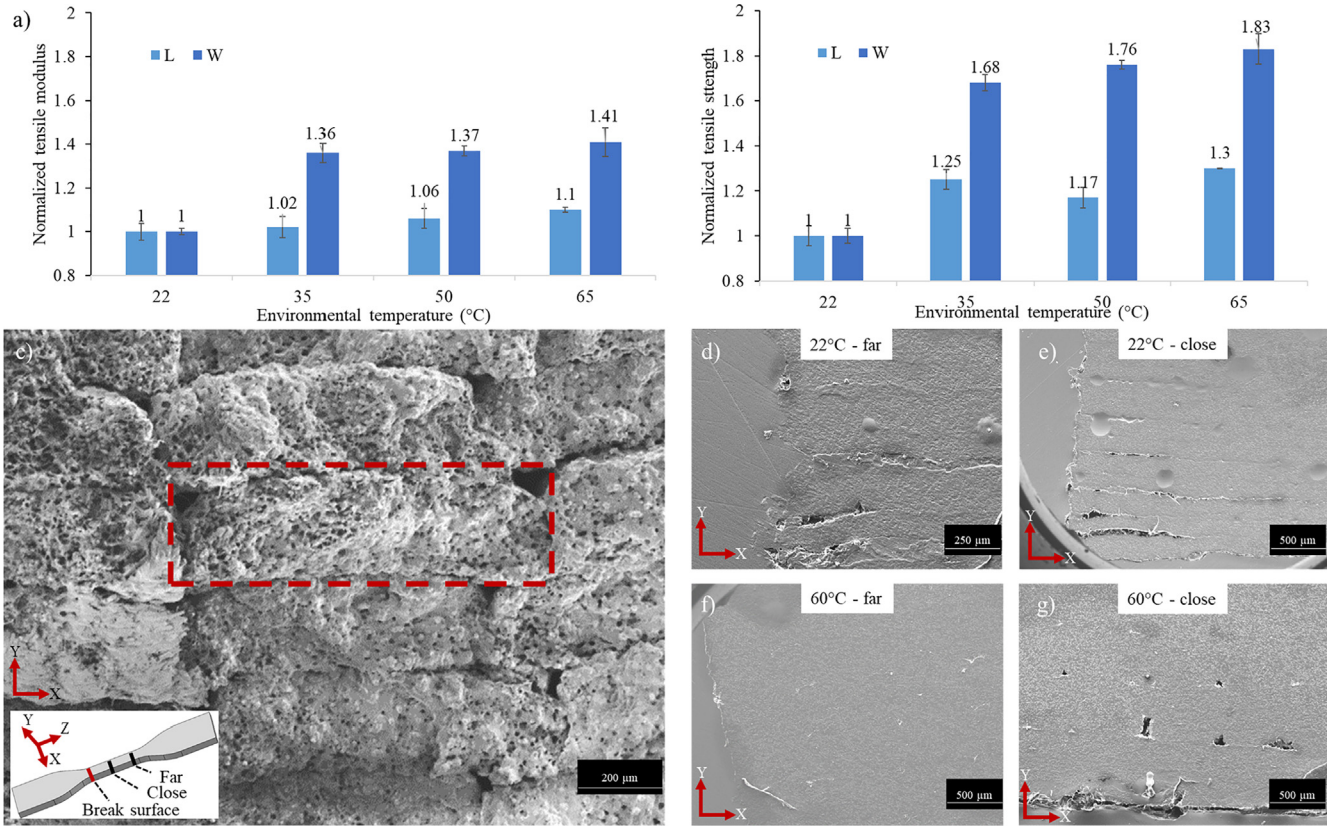

Fig. 6. *Effect of the environmental printing temperature a) Normalized tensile modulus and (b) ultimate tensile strength in* L *and* W *specimen with 35 wt% MCF according to environmental temperature. c) SEM micrographs of the fracture surface of a sample printed at room temperature with an enclosed schematic for the micrograph's placement. A single filament is highlighted with a dashed rectangle d-e) SEM micrographs of a room-temperature printed sample in different sections along the loading direction (d) far and (e) close to the fracture surface. f-g) SEM micrographs of a sample printed at 65 °C in different sections along the loading direction (f) far and (g) close to the fracture surface.*

for 3D printed specimen between filaments, which is a distinct feature for breaking surface of this kind of material. SEM observations were carried out on different sections, as detailed in the schematic in the appendix, to observe the delamination along the specimen's length. Fig. 6.d and 6.e show sections of a 35 wt% CCF-reinforced polyamide specimen printed in the L direction at room temperature labeled "far" (around 25 mm from the break plane) and "close" (around 15 mm from the break plane). Assuming there is no damage occurring at the grips, observation of the filament interfaces at different places can inform about the amount of delamination occurring at the specimen breaking. The SEM micrographs show a more accentuated delamination in the cross section labeled "far", attesting the progressive delamination and filament debonding expected from such a structure. Fig. 6.f and 6.g show the same sections but in a specimen printed at 65 °C. These sections differentiate themselves from those for the room-temperature printed specimens as showing little to no debonding between filaments. While the loading at break was superior for the specimen printed at 65 °C, the filaments did not delaminate as much as in the case of the room-temperature printed specimen, which suggests a stronger interfacial adhesion between filaments for the former case.

CT-scan observations were carried out on CCF-reinforced specimens to visualize the bonding between filaments in pristine specimens. Fig. 7.a shows the two different planes of interest, where the *XZ* plane shows the state of filament through different layers while the *YZ* plane shows the state inside a single layer. In the *XZ* plane scan, a small pore between the layers is observable in the room-temperature case (Fig. 7.b) while porosity could not be detected in the specimen printed at 65 °C. The same observations can be made in the *YZ* plane. The process-related porosity has a strong impact on the mechanical properties of 3D printed samples, and lowering the porosity has a stronger effect on the direction orthogonal to the printing direction, as shown in the mechanical test results. The strength in the direction orthogonal to the filament direction is significantly influenced by the repetitive placement of inter-filament interfaces in the trajectory of the loading.

Because of the heated environment, the deposited layer stays at a temperature closer the glass transition temperature, allowing for a better bonding with the next layer, through molecular diffusion. As molten material is added on top of the previous layer, there is local increase of temperature at the interface. At a higher environmental temperature, the material at the interface goes up more easily to the melting point, thus creating a stronger interface. 3D printer apparatus with a heated environment are marketed for high temperature matrices such as PEI or PEEK, but a heated environment is shown here to have positive impact on mechanical properties of other grades of polymers as well.

4. Conclusion

This study showed that the addition of carbon fibers into a PA12 matrix improves both its stiffness and strength, at the expense of ductility. The type of carbon fibers (i.e., milled or chopped) has a sizable effect on mechanical properties as shown by comparing the different composites and using the predictions of the Mori-Tanaka homogenization model. We report up to a seven-fold increase in tensile modulus (up to 8.8 GPa) and a two-fold increase of strength (up to 90 MPa) at a 35 wt% concentration using chopped carbon fibers with sizing. These results put this material

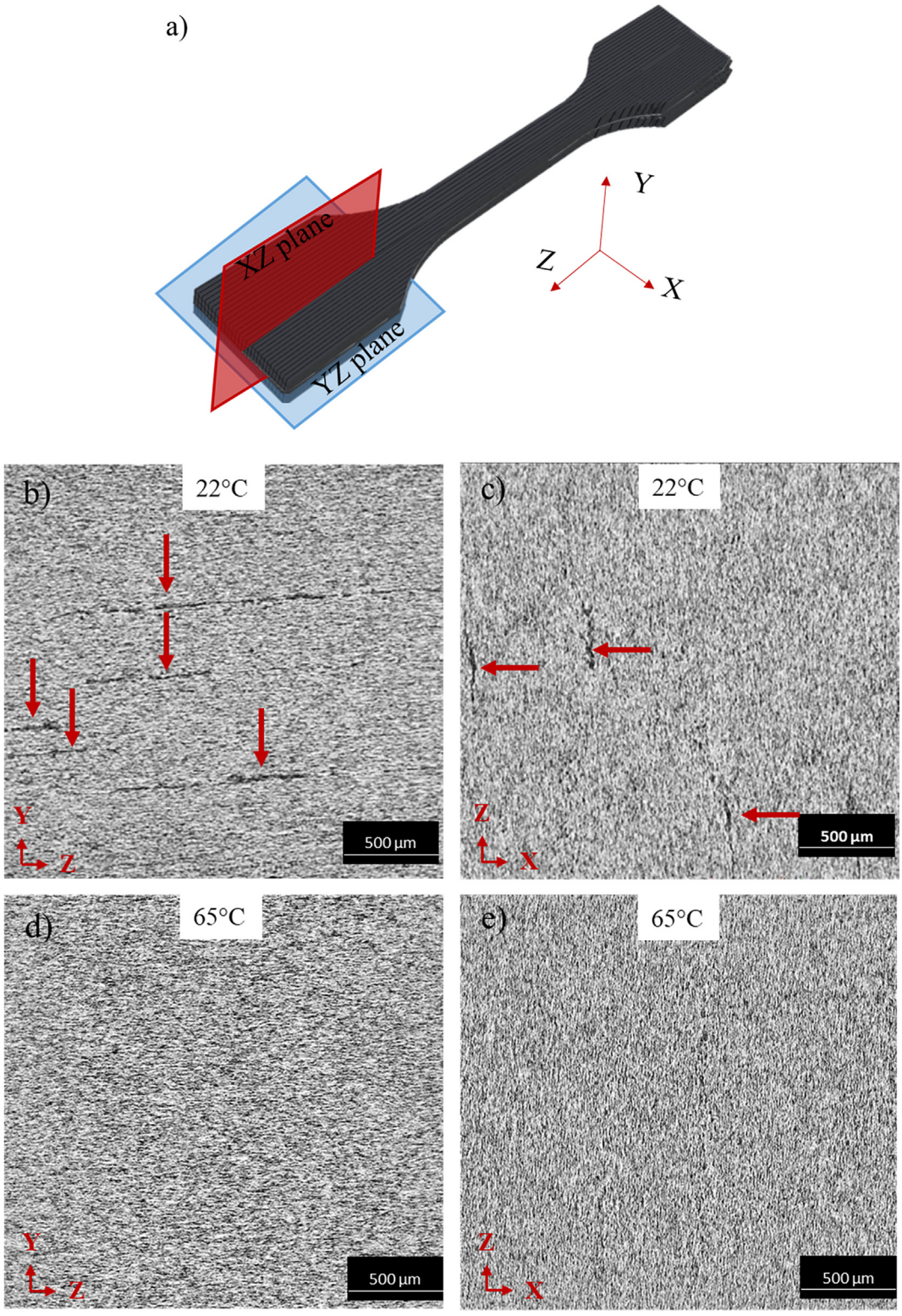

Fig. 7. Plane orientation and images of CT scan of CCF-reinforced printed specimens for interlayer observation. a) Schematic of the planes of the CT scans for the images. b–e) Scans of room temperature printed specimen in b) YZ plane and c) XZ plane and specimen printed at 65 °C in d) YZ plane and e) XZ plane.

among the strongest and stiffest printed short fiber composite, as seen in the benchmark published by Dickson et al. [28]. The study also showed the benefits of using a controlled environmental temperature during printing, mostly on the transverse samples with two-fold increase of the strength. Microscopic observation showed that the effect of heating mainly affects the quality of the bonding between filaments, with samples printed at higher temperature having less porosity and are less prone to delamination during mechanical loading, when compared to the samples printed at room temperature.

5. Data availability

The raw/processed data required to reproduce these findings cannot be shared at this time due to legal reasons and can be made available at an ulterior time.

Declaration of Competing Interest

The authors declare that they have no known competing financial interests or personal relationships that could have appeared to influence the work reported in this paper.

Acknowledgments

This work has been supported through Collaborative Research and Development Grant – Project (CRDPJ) entitled "Advanced manufacturing of composites for structural and acoustic applications", with Safran S.A. (NSERC file number: CRDPJ 514761 – 17).

Appendix A. Supplementary material

Supplementary data to this article can be found online at https://doi.org/10.1016/j.matdes.2021.110358.

References

[1] F. Ning, W. Cong, Z. Jia, F. Wang, and M. Zhang, "Additive Manufacturing of CFRP Composites Using Fused Deposition Modeling: Effects of Process Parameters," no. 49910, p. V003T08A001, 2016
[2] F. Ning, W. Cong, Y. Hu, H. Wang, Additive manufacturing of carbon fiber-reinforced plastic composites using fused deposition modeling: effects of process parameters on tensile properties, J. Compos. Mater. 51 (4) (2017) 451–462.
[3] N.S. Hmeidat, J.W. Kemp, B.G. Compton, High-strength epoxy nanocomposites for 3D printing, Compos. Sci. Technol. 160 (2018) 9–20.
[4] X. Wang, M. Jiang, Z. Zhou, J. Gou, D. Hui, 3D printing of polymer matrix composites: a review and prospective, Compos. B Eng. 110 (2017) 442–458.
[5] H.L. Tekinalp, V. Kunc, G.M. Velez-Garcia, C.E. Duty, L.J. Love, A.K. Naskar, C.A. Blue, S. Ozcan, Highly oriented carbon fiber–polymer composites via additive manufacturing, Compos. Sci. Technol. 105 (2014) 144–150.
[6] C. Yang, X. Tian, D. Li, Y.i. Cao, F. Zhao, C. Shi, Influence of thermal processing conditions in 3D printing on the crystallinity and mechanical properties of PEEK material, J. Mater. Process. Technol. 248 (2017) 1–7.
[7] T.N.A. Tuan Rahim, A.M. Abdullah, H. Md Akil, D. Mohamad, Z.A. Rajion, Preparation and characterization of a newly developed polyamide composite utilising an affordable 3D printer, J. Reinf. Plast. Compos. 34 (19) (2015) 1628–1638.
[8] W. Griehl, D. Ruestem, Nylon-12-preparation, properties, and applications, Ind. Eng. Chem. 62 (3) (1970) 16–22.
[9] J.W. Stansbury, M.J. Idacavage, 3D printing with polymers: challenges among expanding options and opportunities, Dent. Mater. 32 (1) (2016) 54–64.
[10] D.D. Chung, D. Chung, Carbon fiber composites, Elsevier, 2012.
[11] P.K. Mallick, Fiber-reinforced composites: materials, manufacturing, and design, CRC Press, 2007.
[12] A.P. Mouritz, M.K. Bannister, P.J. Falzon, K.H. Leong, Review of applications for advanced three-dimensional fibre textile composites, Compos. A Appl. Sci. Manuf. 30 (12) (1999/12/01/ 1999.) 1445–1461.
[13] Markforged. (2019, May 2019). *Applications - Leverage high-strength 3D printed parts in any stage of the production cycle*. Available: https://markforged.com/applications/#manufacture
[14] N. van de Werken, H. Tekinalp, P. Khanbolouki, S. Ozcan, A. Williams, M. Tehrani, Additively manufactured carbon fiber-reinforced composites: state of the art and perspective, Addit. Manuf. 31 (2020/01/01/ 2020.) 100962.
[15] X. Wang, L. Zhao, J.Y.H. Fuh, H.P. Lee, Effect of porosity on mechanical properties of 3D printed polymers: experiments and micromechanical modeling based on X-ray computed tomography analysis, Polymers 11 (7) (2019) 1154.
[16] P. Biswas, S. Guessasma, J. Li, Numerical prediction of orthotropic elastic properties of 3D-printed materials using micro-CT and representative volume element, Acta Mech. 231 (2) (2020) 503–516.
[17] D. Yao et al., Achieving the upper bound of piezoelectric response in tunable, wearable 3D printed nanocomposites, Adv. Funct. Mater. 29 (42) (2019) 1903866.
[18] Y. Benveniste, A new approach to the application of Mori-Tanaka's theory in composite materials, Mech. Mater. 6 (2) (1987) 147–157.
[19] Y.H. Zhao, G.P. Tandon, G.J. Weng, Elastic moduli for a class of porous materials, Acta Mech. 76 (1-2) (1989) 105–131.
[20] B. Michel, "Mura, T., Micromechanics of Defects in Solids. Second, revised edition. Dordrecht etc., Martinus Nijhoff Publishers 1987. XIII, 587 pp., US $ 162. – /Dfl. 345.-. ISBN 90-247-3343-X (Mechanics of Elastic and Inelastic Solids 3)," *ZAMM - Journal of Applied Mathematics and Mechanics / Zeitschrift für Angewandte Mathematik und Mechanik*, vol. 69, no. 2, pp. 66-66, 1989
[21] E. Grivory, "Grilamid L20 Nat - Pa12 Datasheet," PDF file 2017-08-02 2017.
[22] P. Virtanen et al., "SciPy 1.0: fundamental algorithms for scientific computing in Python," (in eng), Nat Methods 17 (3) (Mar 2020) 261–272.
[23] D.M. Bigg, Effect of compounding on the properties of short fiber reinforced injection moldable thermoplastic composites, Polym. Compos. 6 (1) (1985) 20–28.
[24] D. Cho, S.H. Yun, J. Kim, S. Lim, M. Park, S.-S. Lee, G.-W. Lee, Influence of silane coupling agents on the interlaminar and thermal properties of woven glass fabric/nylon 6 composites, *Macromol. Res.* journal article 12 (1) (2004) 119–126.
[25] J.J. Martin, M.S. Riederer, M.D. Krebs, R.M. Erb, Understanding and overcoming shear alignment of fibers during extrusion, Soft Matter 11 (2) (2015) 400–405, https://doi.org/10.1039/C4SM02108H.
[26] H. Miyagawa, T. Mase, C. Sato, E. Drown, L.T. Drzal, K. Ikegami, Comparison of experimental and theoretical transverse elastic modulus of carbon fibers, Carbon 44 (10) (2006/08/01/ 2006.) 2002–2008.
[27] K. Rodzeń, E. Harkin-Jones, M. Wegrzyn, P.K. Sharma, A. Zhigunov, Improvement of the layer-layer adhesion in FFF 3D printed PEEK/carbon fibre composites, Compos. A Appl. Sci. Manuf. 149 (2021/10/01/ 2021.) 106532.
[28] A.N. Dickson, H.M. Abourayana, D.P. Dowling, 3D printing of fibre-reinforced thermoplastic composites using fused filament fabrication—a review, Polymers 12 (10) (2020) 2188.